

Fast and slow surfactants in turbulent bubble breakup

Zhan Wu^{1*}, Tristan Aurégan^{1*}, and Luc Deike^{1,2}

¹Department of Mechanical and Aerospace Engineering, Princeton University, Princeton, NJ, USA

² High Meadows Environmental Institute, Princeton University, Princeton, NJ, USA

Abstract

When a large air cavity breaks in a turbulent flow, it goes through very large deformations and cascading events of new interface formation, including elongated filaments and bubbles over a wide range of scales, with their rate of formation controlled by turbulence and capillary processes. We experimentally investigate the effects of surfactants and salt on the fragmentation, and observe an order of magnitude increase of the number of bubbles being produced in some cases. For bubbles larger than the Hinze scale d_H (defined as the balance between surface tension and turbulence stresses), we observe that bubble size distributions remain unchanged for all solutions tested. For bubbles below d_H , however, we observe an increase of the number of bubbles produced and an associated steepening of the bubble size distribution upon the addition of surfactant or salt. This later effect is only visible for some of the surfactants tested when their adsorption timescale is fast enough compared to the rate at which new interfaces are being generated by turbulence.

1 Introduction

Gas bubbles dispersed in turbulent flows play a crucial role in mediating the transfer of mass and energy across interfaces. At the ocean surface the bursting of bubbles produces sea spray aerosols (Deike, 2022; Deike et al., 2022; Cochran et al., 2017), influencing atmospheric and climate processes, while bubbles entrained underwater break (Deike et al., 2016; Deane and Stokes, 2002) and influence gas exchange (Deike and Melville, 2018; Deike, 2022; Deike et al., 2025). Underwater bubbles transport facilitates oil and gas migration from deep wells, while bubble breakup enhances gas dissolution through increased interfacial area and enhanced mixing in bubble column reactors (Galinat et al., 2005; Risso, 2018).

In practical configurations, air-water interfaces are almost always contaminated by surface active agents (surfactants) related to biological or anthropogenic activities. The presence of surfactant modulates surface waves dynamics (Erin et al., 2023a), bubble rise velocity (Takemura and Yabe, 1999; Tagawa et al., 2014; Farsoiya et al., 2024), bubble bursting (Eshima et al., 2025), with surface tension gradients leading to Marangoni flows, as well as tip streaming leveraged in microfluidics devices to produce droplets (Eggleton et al., 2001; Rubio and Montanero, 2023). Another practical example of surfactant effects include oil-contaminated surfaces, where surfactants are used in mitigation strategies but also lead to chemical transport by aerosolization (Sampath et al., 2019; Yang et al., 2023). Beyond Marangoni effects, variations in surface tension and sorption kinetics also play important roles

*Author contributions: Z.W. and T.A. contributed equally to this work.

(Fernández-Martínez et al., 2025), and comparison between the time scale of adsorption/desorption of surfactant molecules with the characteristic time scale of the flow of interest becomes necessary. A comprehensive understanding of surfactant-mediated bubble behavior is essential for both mitigating environmental impacts of marine pollution and optimizing industrial processes involving gas–liquid interactions.

In this letter, we consider the effect of surfactant on bubble break-up. Bubble fragmentation under breaking waves or in turbulent flows has been widely investigated through both experiments (Deane and Stokes, 2002; Ruth et al., 2022; Ni, 2024) and numerical approaches (Deike et al., 2016; Mostert et al., 2022; Rivière et al., 2021, 2022). Some numerical studies have probed the effect of surfactants in two-phase turbulence (Soligo et al., 2019; Cannon et al., 2024), and a few experiments investigated the role of salt in bubbly flows (Blaauw et al., 2025), but to the best of our knowledge, no systematic studies on the role of surfactants on the distribution of bubbles in turbulence exist.

Bubble breakup in turbulence is initially understood by considering the competition between inertial stresses from turbulence that promote fragmentation and surface tension forces that resist it. The Weber number, $We = \rho U^2 d / \gamma$, which compares these two effects, is commonly used to characterize bubble breakup conditions. Here, d is the bubble's volume-equivalent diameter, U a characteristic velocity defined as the average velocity difference at the bubble-diameter scale, ρ the liquid density, and γ_s the surface tension. For bubbles within the inertial subrange, the square of the characteristic velocity at the bubble scale is $2\epsilon^{2/3}d^{2/3}$, leading to $We = 2\rho\epsilon^{2/3}d^{5/3}/\gamma$ Rivière et al. (2021). A critical Weber number We_c provides the balance between inertial and surface tension forces, serves as a loose bubble breakup criterion and is of order unity (Martínez-Bazán et al., 1999; Vejrazka et al., 2018; Rivière et al., 2021). The associated length scale is the Hinze scale, d_H (Hinze, 1955):

$$d_H = \left(\frac{We_c}{2} \right)^{3/5} \left(\frac{\gamma_s}{\rho} \right)^{3/5} \epsilon^{-2/5}, \quad (1)$$

which separates the super-Hinze regime ($d > d_H$) which will break due to turbulence, from the sub-Hinze regime ($d < d_H$). The critical Weber number or Hinze scale is a soft threshold due to the inherent stochasticity of turbulent flows. The super-Hinze bubble size distribution in turbulence or under breaking waves has been described by $N(d) \propto d^{-10/3}$, explained by a turbulent break-up cascade, controlled by the eddy turn over time at the scale of the bubble $T_{\text{eddy}}(d) = \epsilon^{-1/3}d^{2/3}$ (Garrett et al., 2000). In contrast, the sub-Hinze bubble size distribution exhibits a gentler slope, following $N(d) \propto d^{-3/2}$, which can be explained by a capillary break-up process related to large bubbles experiencing large deformation and the formation of filaments which will then rupture in a time scale controlled by capillarity $T_{\text{cap}}(d) = (2\sqrt{3})^{-1}(\rho/\gamma_s)^{1/2}d^{3/2}$ (Rivière et al., 2022; Ruth et al., 2022). Both regimes have been extensively documented through laboratory experiments (Ruth et al., 2022; Deane and Stokes, 2002) and direct numerical simulations (Mostert et al., 2022; Rivière et al., 2022). The formation of such broad size distribution from an initial air cavity occurs through a sequence of events controlled by the turbulent and capillary time scales, with new interfaces formed along the way.

Figure 1 (a) illustrates the time scales of bubble break-up in turbulence as a function of bubble size d , using the integral length scale and turbulent dissipation rate estimated in our laboratory experiments. The lengths are normalized by the integral length scale L_{int} , corresponding to the length scale of the largest eddies (≈ 1 cm) and the times are normalized by the associated integral timescale ($T_{\text{int}} \approx 40$ ms).

When using surfactants, we now have to consider their relevant time scales and how they compare to capillary and turbulence times which will control break-up and deformation. Marangoni stresses related to gradients in surfactant concentration along the interface will occur on capillary time scales.

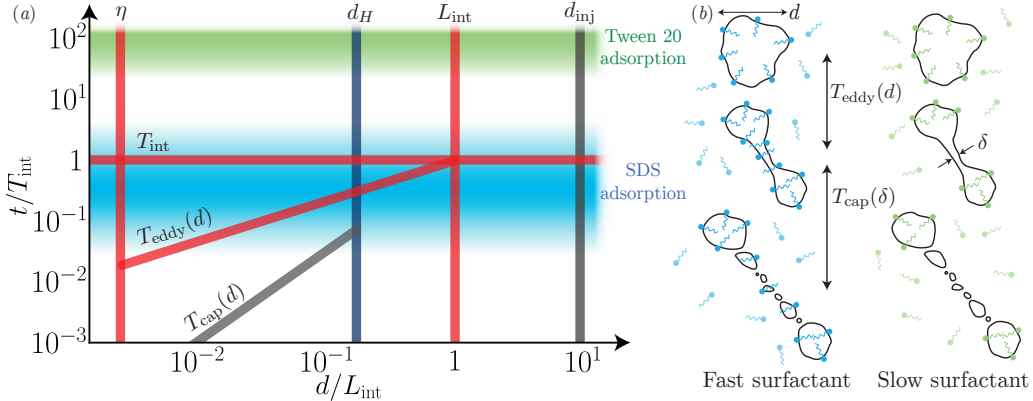


Figure 1: (a) Comparisons of the timescales of turbulence, capillary instability and adsorption of both surfactants used in this study. The length scales are normalized by the integral length scale of turbulence L_{int} and the time scales by the integral time T_{int} . η is the Kolmogorov scale and d_{inj} is the equivalent diameter of the volume of air initially injected. (b) Schematic of the adsorption dynamics of a fast or slow surfactant during the break-up process. A bubble of size d initially covered with surfactants is stretched forming filaments, over a typical time $T_{\text{eddy}}(d)$. The air filament of radius δ fragments into small bubbles in a time of the order $T_{\text{cap}}(\delta)$.

However, the presence and amount of surfactant on a newly formed interface within a sequence of break-up events will be related to the surfactant adsorption time τ_{ads} , which controls how fast surfactant in the bulk will make it to the interface (Manikantan and Squires, 2020). As we will demonstrate experimentally, surfactant will influence the multi-scale break-up processes in different ways depending on the characteristic adsorption time of the surfactant, illustrated for Sodium Dodecyl Sulfate (SDS, short adsorption) and Tween 20 (fast adsorption) in figure 1 (a). For SDS, which has a short adsorption time of the order of milliseconds to tenths of seconds depending on the concentration (Chang and Franses, 1995; Fainerman et al., 2010), the sorption dynamics will be occurring over a time scale comparable to T_{eddy} , allowing SDS molecules to adsorb onto the surface of newly formed bubbles or ligaments and influence the breakup process. However, the capillary instability leading to the final break-up will occur on time scales faster than the adsorption. In contrast for Tween 20, which has a long adsorption time of the order of tens of seconds (Bak and Podgórska, 2016; Qazi et al., 2020), T_{eddy} and T_{cap} are generally shorter than its adsorption time, leaving insufficient time for adsorption during a single set of breakup event. This observation (illustrated in fig. 1b) will guide the interpretation of our experiments varying surfactant concentration leading to comparable changes in the static surface tension.

The paper is organized as follows. Section 2 presents the experimental techniques while Section 3 presents the resulting bubble size distributions, the are discussed in Section 4.

2 Experimental Set-up

Figure 2 (a) shows the schematic diagram for the experimental setup, similar to Ruth et al. (2022). It consists of a polycarbonate tank filled with about 150L of solution, and a hollow hemispherical metal cup is positioned underwater at the tank center, equidistant from the four corners of the tank where four pumps (Rule 20 DA 800 GPH Bilge Pump) are mounted. The cup initially faces downwards and is filled with a constant volume $V_0 = 20$ mL of air. At the beginning of an experiment, the cup

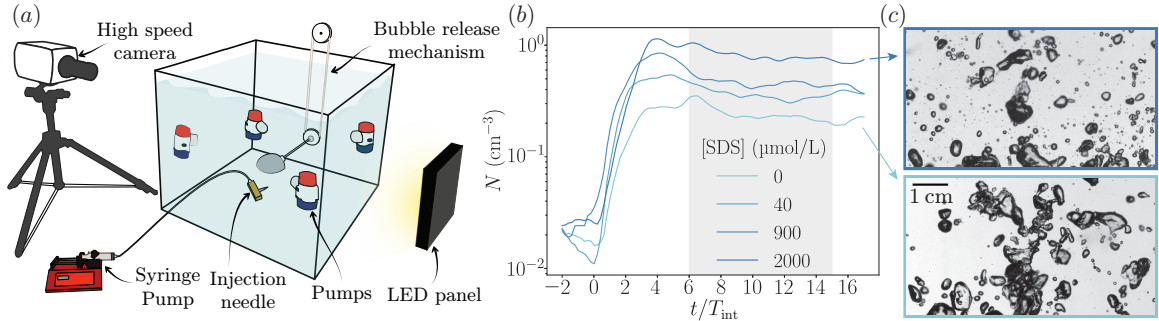


Figure 2: (a) Schematic of the experimental setup: air is injected into an upside down cup that is flipped at the beginning of the experiment, and a large air cavity is released into the turbulent flow. (b) Temporal evolution of the total bubble count N for different SDS concentrations in deionized water. The shaded area represents the range used to compute distributions in the following. (c) Example of images comparing clean (light blue, bottom), and contaminated cases (dark blue, top, 2000 $\mu\text{mol/L}$ of SDS). More small bubbles are produced in presence of SDS.

is rotated to face upwards while a fast camera (Phantom VEO4K-990-L, 500 fps) is simultaneously triggered. The air cavity is released into the turbulent flow and experiences a sequence of breakup which results in a broad distribution of bubble sizes. The high-speed camera is coupled with two different lenses—a wide angle view (Nikon Micro 200mm leading to 35 $\mu\text{m}/\text{pixel}$) and a zoomed-in view (K2 DistaMax Infinity Photo-Optical Co. lens leading to 9 $\mu\text{m}/\text{pixel}$)—and illuminated by a coaxial LED panel from the opposite side. To ensure statistical convergence of the size distribution, each experimental condition is repeated 15 times using the wide-angle lens and 25 times using the K2 lens. The depth of field $\delta(d)$ was calibrated by translating a target containing 14 chrome-sputtered dots with diameters ranging from 30 μm to 3000 μm along the optical axis, similarly to [Erin et al. \(2023b\)](#). We obtain the bubble size distribution $N(d)$ from image processing (two step: thresholding for larger bubbles then edge detection for smaller ones), defined as the number of bubbles per unit bin size $[d, d + \Delta d]$, normalized by the cross sectional area A of the camera and the depth of field at that given size bin $\delta(d)$, and averaged over all realizations. The distributions from the two camera views are combined into a single distribution (see [Mazzatorta et al. \(2025\)](#)). The uncertainties in the distribution is estimated by a Monte Carlo approach in which data are randomly sampled from the repeated experiments using bootstrapping (100 realizations).

We investigate the bubble break-up in four solutions of increasing surfactant concentration: SDS in deionized (DI) water, SDS in artificial seawater (same as in [Mazzatorta et al. \(2025\)](#)), Tween-20 in DI water, and SDS in tap water, summarized in Table 1. For each case, the solution's surface tension isotherm was measured at the beginning and end of the experiment using a Langmuir trough (KSV NIMA 1003), and the static surface tension prior to surface compression was recorded as γ_s . During all experiments, the tank was sealed with an acrylic lid to minimize contamination from ambient air. The choice of solution was made to explore the importance of salt, as well as surfactants with very different adsorption time (SDS: fast; Tween 20: slow) as illustrated in figure 1.

The turbulent properties of the flow are determined from Particle Image Velocimetry (PIV) measurements (using the autocorrelation function to obtain the integral length scale and the scaling argument method to obtain the dissipation rate, similarly to [Ruth et al. \(2022\)](#)). The integral length scale is $L_{\text{int}} = 1.4 \text{ cm}$ (10%: 1.2, 90%: 1.6), the root-mean-square velocity is $u' = 34 \text{ cm/s}$ (10%: 28, 90%: 42), giving a dissipation rate $\varepsilon = 1.9 \text{ m}^2 \text{ s}^{-3}$ (10%: 1.1, 90%: 3.7) where the value reported is the median of the spatial distribution and the values in parentheses are the quantiles, showing some

| Surfactant | Solvent | Concentration (% CMC) | γ_s (mN/m) | d_H (mm) | d_{32} (mm) |
|------------|----------------------|-----------------------|-------------------|------------|---------------|
| SDS | DI water | 0–80 | 70–37 | 1.1–1.6 | 4.4–5.4 |
| SDS | artificial sea water | 0–1.2 | 65–39 | 1.1–1.5 | 4.4–5.7 |
| Tween20 | DI water | 0–100 | 72–41 | 1.2–1.7 | 5.7–6.1 |
| SDS | tap water | 0–2 | 72–55 | 1.3–1.8 | 5.7–6.5 |

Table 1: Summary of surfactant and solvent conditions tested in the study, with the corresponding evolution of the measured static surface tension γ_s , the Hinze scale d_H computed using (1), and the Sauter mean diameter of the measured distributions d_{32} . Concentrations are given as a fraction of the Critical Micelle Concentration (CMC): 8200 $\mu\text{mol/L}$ for SDS and 59 $\mu\text{mol/L}$ for Tween 20.

inhomogeneity in our setup. The associated Kolmogorov scale is 27 μm and the integral timescale is $T_{\text{int}} = 40$ ms. The Hinze scale (eq. (1)) is estimated from the turbulence properties and reported in table 1. The Sauter mean diameter, representative of the large bubbles in the system, does not vary across solutions.

Figure 2(b) presents the temporal evolution of the bubble count, $N = \int \mathcal{N}(d)dd$, for experiments conducted with varying concentrations of SDS in deionized water. Across all experimental conditions, N exhibits a sharp increase immediately after the cup is flipped ($t = 0$), followed by a quasi-steady plateau over the interval $6T_{\text{int}} \leq t \leq 15T_{\text{int}}$. The total number of recorded bubbles increases with the concentration of SDS by almost an order of magnitude. Figure 2(c) compares images of the clean case (pure deionized water) and a contaminated case ($[\text{SDS}] = 2000 \mu\text{mol/L}$) at $t = 10T_{\text{int}}$. The scale bar represents 1 cm. A substantial increase in the number of small bubbles is observed in the contaminated case, whereas the population of large bubbles remains nearly unchanged. Similar observations are made when considering the other types of solutions in terms of time evolution. In the case of DI water with Tween 20, the total number of bubbles is very similar across all contaminations, a feature we will discuss in details when considering the bubble size distribution.

3 Effect of surfactant on bubble production across scales

We now analyze the effect of surfactants on the bubble size distribution resulting from the fragmentation of large air cavities.

3.1 Bubble size distribution

Figure 3 presents the bubble size distribution $\mathcal{N}(d)$ for three of the tested solutions: SDS with DI water (a), SDS with artificial seawater (b), and Tween20 with DI water (c) at increasing surfactant concentrations. The dashed lines are shown as references for the $-10/3$ scaling in the super-Hinze regime and the $-3/2$ scaling in the sub-Hinze regime. The observed transition between these two regimes in the bubble size distribution occurs at $d \approx 2.5$ mm, which is close to the calculated Hinze scale, and is used as effective Hinze scale $d_{H,\text{eff}}$.

For a given set of experiments, the distribution in the super-Hinze scale range ($d > d_{H,\text{eff}}$) does not change when adding surfactants, and is very similar across the different solutions tested. As the concentration of SDS is increased, either with DI water (Figure 3(a)) or artificial seawater (Figure 3(b)), the total number of bubbles in the sub-Hinze range increases while that in the super-Hinze regime remains unchanged. The increase in the number of bubbles in the sub-Hinze range is associated

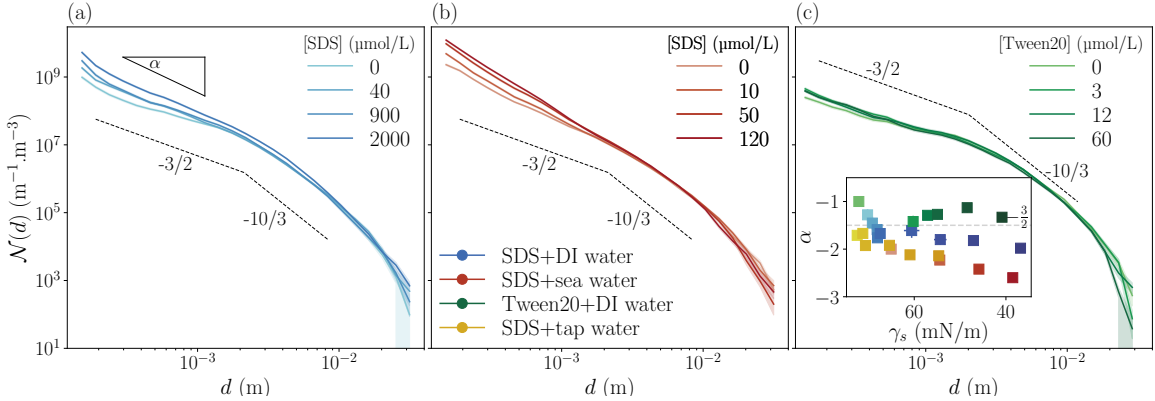


Figure 3: Comparison between the bubble size distributions of different solution composition at varying surfactant concentration. Bubble size distribution for (a) DI water and SDS; (b) artificial sea water and SDS; (c) DI water and Tween20. The shaded areas correspond to uncertainties on the distributions, computed using a Monte Carlo approach. (inset) Comparison of the fitted exponents α of the power law in the sub-Hinze regime for the four solution compositions at varying surfactant concentrations.

with an increase in the slope of the distribution. In contrast, when Tween20 is added to DI water (Figure 3(c)), the bubble size distribution remains unchanged both in the super-Hinze and sub-Hinze ranges. Details of the solution (salt, surfactant) only affect sub-Hinze scale bubbles, the effect strongly dependent on the type of surfactant used, while the super-Hinze size distribution remains unchanged.

Considering $d_{H,\text{eff}} \approx 2.5\text{mm}$, we fit power laws $N(d) \propto d^\alpha$ for the sub-Hinze regime ($d < d_{H,\text{eff}}$). The inset in Figure 3 (c) shows the variation of the fitted slopes α . For all conditions, the exponent at the lowest contamination is compatible with the $d^{-3/2}$ distribution due to capillary break-up, as visible in the size distribution plots, and compatible with data in Ruth et al. (2022). For SDS in DI water (blue), artificial seawater (red), and tap water (yellow), the fitted slopes α become more negative as contamination increases (quantified here with the surface tension) whereas for Tween20 in DI water (green), the slope remains nearly constant. These observations are consistent with visual observation of the distributions which do not show changes for Tween20 across surfactant concentrations while more bubbles are observed in the sub-Hinze regime for SDS solutions. Note that this observed deviation of the exponent of the power-law in the sub-Hinze regime rules out the possibility that the trends observed in this study are merely a result of increasing the Weber number through a change of the static surface tension. Indeed, if this was the case, the whole distribution would be shifted upwards, with the same exponent $-3/2$ in the sub-Hinze regime. Instead, we expect Marangoni effects during the capillary instability of the air filaments to play a key role in setting the distribution.

3.2 Counts of Super-Hinze and Sub-Hinze bubbles

We now quantify the increase of sub-Hinze bubbles ($N_{d < d_H}$) for the various cases and in particular the limits of a fast surfactant (SDS) versus a slow surfactant (Tween20).

Figure 4(a) shows the counts of super-Hinze bubbles $N_{d > d_H}$ (open triangles) and sub-Hinze bubbles $N_{d < d_H}$ (full squares) as contamination increases (represented as the static surface tension, note the inverted x-axis) for the different types of contamination (colors).

As contamination increases with the addition of surfactant (surface tension is reduced), the super-Hinze bubble count remains unchanged in all cases (triangles). For sub-Hinze bubbles, all solutions

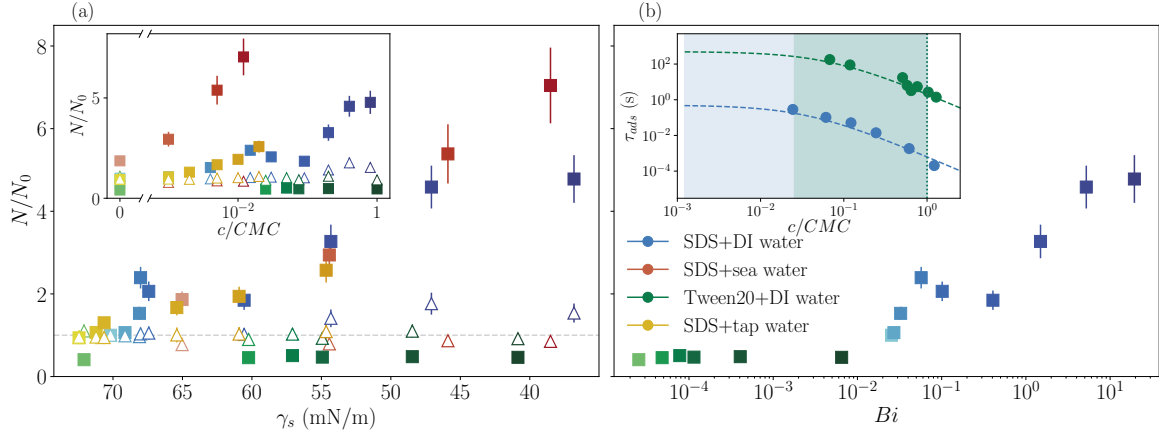


Figure 4: (a) Variation in the counts of super-Hinze (open triangles) and sub-Hinze (solid squares) bubbles with surface tension. Colors—blue, red, green, and yellow—represent the cases of SDS + DI water, SDS + artificial seawater, Tween20 + DI water, and SDS + tap water, respectively. (inset) Same data as a function of the bulk concentration of surfactant, represented as a fraction of the CMC. (b) Variation in the counts of sub-Hinze bubbles with the Biot number Bi , for SDS and Tween 20 in DI water only. (inset) Adsorption time τ_{ads} as a function of bulk concentration of surfactant in solution. Data points are from the literature, shaded areas represent the ranges used in this study and vertical dashed lines represent the CMC. Blue for SDS (Fainerman et al., 2010) and green for Tween 80 (Qazi et al., 2020).

with a fast surfactant (SDS, i.e. blue, red and yellow squares) show an increase in counts: for very low surface tensions, the number of sub-Hinze bubbles is increased by almost an order of magnitude. In contrast, for cases where surface tension is modified by adding a slow surfactant (Tween20, green squares) to DI water, the sub-Hinze bubble counts remain unchanged. The addition of salt (red) or the use of non pure water (yellow) still is associated with a similar increase in the number of sub-Hinze bubbles as the contamination is increased. However, the concentration of surfactants required to obtain a similar increase in number can be vastly different (see inset), suggesting a reinforcement of the effect of SDS (anionic) upon the addition of ions. This effect relatively well captured by plotting the counts as a function of the static surface tension.

As stated above, the various cases with Tween20 show no differences with clean DI water despite a factor 2 reduction in surface tension, comparable to the reduction when using SDS in DI water or seawater, further highlighting that the increase in the number of sub-Hinze bubbles and the change in the power law observed here is not simply due to a reduction in surface tension and associated increase in Weber number.

As hinted in the introduction and now demonstrated experimentally, the influence of surfactant on the break-up process is tightly linked to their adsorption time. Surfactants will only affect the breakup process if a significant amount can adsorb to the interface of a bubble between two successive fragmentation events. Indeed, during the stretching preceding fragmentation, a large amount of surface area is created and therefore the surfactant surface concentration on a newly formed bubble is less than the value at equilibrium with the bulk (see sketch in figure 1 (b)). If the timescale for adsorption of surfactants to the interface τ_{ads} is much longer than the typical time between fragmentation events, then after a few breakups, the bubbles will essentially behave as clean bubbles by successive dilutions. To quantify this effect, we introduce the Biot number (Tasoglu et al., 2008; Pico et al., 2024), comparing

the typical time between breakup events $T_{\text{eddy}}(d)$ to the adsorption timescale:

$$Bi = \frac{T_{\text{eddy}}(d)}{\tau_{\text{ads}}} \quad (2)$$

In the following, we use $d_{H,\text{eff}} \simeq 2.5$ mm as a typical length scale to compute the Biot number (a different value would simply shift the estimated Bi without changing our conclusions). We need to estimate the adsorption timescale for the various contamination cases considered. The inset of Fig. 4(b) shows data from the literature for SDS (extracted from (Fainerman et al., 2010)) and Tween 80 (a surfactant similar to Tween 20 but with more oxyethylene groups, extracted from (Qazi et al., 2020)). Both datasets are measured using a Maximum Bubble Pressure Tensiometer, and Tween 80 has a much slower adsorption (~ 10 s) than SDS (~ 10 ms). Note however that the datasets cover concentrations that are larger than the ones we use (highlighted with the shaded areas). We therefore need to model the adsorption timescales at lower concentrations.

We follow the approach detailed by Ferri and Stebe (2000): under the assumption that the adsorption is diffusion limited, the adsorption timescale can be expressed as $\tau_{\text{ads}} \sim h^2/D$, where D is the diffusivity of the surfactant and h is the depletion depth, the thickness of the layer depleted of surfactants below the interface. This depth is then given by $h = \Gamma/c$, with c the bulk concentration and Γ the surface concentration at equilibrium, which is not directly accessible but given by the isotherm (or surfactant equation of state) that the surfactant follows. We make the hypothesis that both surfactants follow a Langmuir isotherm, in which case $\Gamma(c) = \Gamma_\infty K c / (1 + K c)$, with Γ_∞ and K two constants. Bringing these results together, we obtain finally that the adsorption timescale should follow $\tau_{\text{ads}} = t_0 / (1 + c/c_0)^2$, with t_0 and c_0 two fitting parameters. This functional form fits well the available literature data, in particular the c^{-2} scaling observed in both datasets (dashed lines). Note however that the approach that we use here is only done to extract a typical adsorption time and has several limitations: first, we have no proof that the adsorption is indeed diffusion limited and that kinetics do not start to play a role for some of the concentrations (although if diffusion is the limiting factor, one expects the c^{-2} scaling observed in the data (Ward and Tordai, 1946)). Second, both datasets were recorded in quiescent conditions, whereas in our case turbulence constantly mixes the fluid and brings surfactant close to the interface. As a consequence, diffusion may be significantly faster than expected (or the depletion depth thinner) and adsorption kinetics may play a role (Chang and Franses, 1995).

We finally plot the normalized count of sub-Hinze bubbles as a function of the Biot number, computed using the fitted adsorption timescale in Fig. 4(b). As expected, we now very clearly see two different regimes: at very low Bi , the surfactant is too slow to adsorb up to a significant amount between breakup events and as a consequence the dynamics is identical to the clean case ($N/N_0 \approx 1$). At higher Bi however, the number of sub-Hinze bubbles progressively increases as a significant amount of surfactants can adsorb to bubbles before they fragment through the capillary instability, during which important surface tension gradients can then form and influence the resulting size distribution.

4 Conclusion

Surface active compounds can have a very large impact on bubble breakup in turbulence: they drastically increase the production of sub-Hinze scale bubbles (up to an order of magnitude) while leaving the super-Hinze range unchanged. The size distribution of bubbles is modified with the sub Hinze part of the distribution still well described by a power law, but with an exponent increasingly

more negative than $-3/2$ as the contamination of the solution is increased. However not all surfactants have the effects described above. As demonstrated experimentally, Tween 20, despite reducing the surface tension by a factor two, has strictly no effect on the size distribution of bubbles. This striking difference is due to the slow adsorption of this surfactant compared with the eddy turnover time, quantified with the Biot number. The addition of ions in the solution reinforces the effects of SDS and a concentration a hundred times smaller can have the same effect on the breakup process as SDS only, when artificial sea salt is added, for comparable static surface tension. Our results demonstrate however that static surface tension can't be the only parameter to discuss effects on fragmentation. In other interfacial fluid dynamics problems, we highlighted the importance of Marangoni effects and gradients in surface tension that can be characterized by Langmuir trough measurement of isotherms under compression (Erin et al., 2023a; Eshima et al., 2025). Here the measured isotherms for the Tween20 or SDS solutions are fairly similar and a metric based on the Marangoni number alone would not explain the differences in the sub-Hinze bubble production. The common denominator between the problems cited above is that the problem could be treated by considering an initially contaminated interface with insoluble surfactants. Because of the successive fragmentations that bubbles will undergo during the experiment and the multiscale nature of turbulence, this approach is not sufficient here. It therefore remains an open problem to find the right sets of parameter to fully describe a solution and predict the final size distribution of bubbles which should take into account the surfactants adsorption time, possible ionic interactions, and the ability for a given surfactant to generate strong Marangoni flows.

Declaration of Interests. The authors report no conflict of interest.

Acknowledgements. We thank Emmy Roy who conducted preliminary experiments.

Funding. This work was supported by NSF grant 2242512 to L.D.

References

- Bak, A. and Podgórska, W. (2016). Interfacial and surface tensions of toluene/water and air/water systems with nonionic surfactants tween 20 and tween 80. *Colloids and Surfaces A: Physicochemical and Engineering Aspects*, 504:414–425.
- Blaauw, L. J., Lohse, D., and Huisman, S. G. (2025). Salts promote or inhibit bubbly drag reduction in turbulent taylor–couette flows. *International Journal of Multiphase Flow*, 184:105078.
- Cannon, I., Soligo, G., and Rosti, M. E. (2024). Morphology of clean and surfactant-laden droplets in homogeneous isotropic turbulence. *Journal of Fluid Mechanics*, 987:A31.
- Chang, C. and Franses, E. I. (1995). Adsorption dynamics of surfactants at the air/water interface: a critical review of mathematical models, data, and mechanisms. *Colloids and Surfaces A: Physicochemical and Engineering Aspects*, 100:1–45.
- Cochran, R. E., Ryder, O. S., Grassian, V. H., and Prather, K. A. (2017). Sea spray aerosol: the chemical link between the oceans, atmosphere, and climate. *Accounts of Chemical Research*, 50(3):599–604.
- Deane, G. B. and Stokes, M. D. (2002). Scale dependence of bubble creation mechanisms in breaking waves. *Nature*, 418(6900):839–844.
- Deike, L. (2022). Mass transfer at the ocean–atmosphere interface: The role of wave breaking, droplets, and bubbles. *Annual Review of Fluid Mechanics*, 54:191–224.

Deike, L. and Melville, W. K. (2018). Gas transfer by breaking waves. *Geophysical Research Letters*, 45:10482–10492.

Deike, L., Melville, W. K., and Popinet, S. (2016). Air entrainment and bubble statistics in breaking waves. *Journal of Fluid Mechanics*, 801:91–129.

Deike, L., Reichl, B. G., and Paulot, F. (2022). A mechanistic sea spray generation function based on the sea state and the physics of bubble bursting. *AGU Advances*, 3.

Deike, L., Zhou, X., Rustogi, P., Stanley, R., Reichl, B. G., Bushinsky, S., and Resplandy, L. (2025). A universal wind–wave–bubble formulation for air–sea gas exchange and its impact on oxygen fluxes. *Proceedings of the National Academy of Sciences*, 122.

Eggleton, C. D., Tsai, T., and Stebe, K. J. (2001). Tip streaming from a drop in the presence of surfactants. *Physical review letters*, 87(4):048302.

Erinin, M. A., Liu, C., Liu, X., Mostert, W., Deike, L., and Duncan, J. H. (2023a). The effects of surfactants on plunging breakers. *Journal of Fluid Mechanics*, 972:A23.

Erinin, M. A., Néel, B., Mazzatorta, M. T., Duncan, J. H., and Deike, L. (2023b). Comparison between shadow imaging and in-line holography for measuring droplet size distributions. *Experiments in Fluids*, 64.

Eshima, J., Aurégan, T., Farsoiya, P., Popinet, S., Stone, H., and Deike, L. (2025). Size amplification of jet drops due to insoluble surfactants.

Fainerman, V. B., Llylyk, S. V., Aksenenko, E. V., Petkov, J. T., Yorke, J., and Miller, R. (2010). Surface tension isotherms, adsorption dynamics and dilatational visco-elasticity of sodium dodecyl sulphate solutions. *Colloids and Surfaces A*, 354(1–3):8–15.

Farsoiya, P. K., Popinet, S., Stone, H. A., and Deike, L. (2024). Coupled volume of fluid and phase field method for direct numerical simulation of insoluble surfactant-laden interfacial flows and application to rising bubbles. *Phys. Rev. Fluids*, 9:094004.

Fernández-Martínez, D., Vega, E. J., M., M. J., J., G.-H. U., and D., F. R. (2025). Influence of surfactant kinetics on rapid interface creation via microjet impact on liquid pools. *arXiv preprint arXiv:2510.25469*.

Ferri, J. K. and Stebe, K. J. (2000). Which surfactants reduce surface tension faster? a scaling argument for diffusion-controlled adsorption. *Advances in Colloid and Interface Science*, 85(1):61–97.

Galinat, S., Masbernart, O., Guiraud, P., Dalmazzone, C., and Noïk, C. (2005). Drop break-up in turbulent pipe flow downstream of a restriction. *Chemical Engineering Science*, 60(23):6511–6528.

Garrett, C., Li, M., and Farmer, D. (2000). The connection between bubble size spectra and energy dissipation rates in the upper ocean. *Journal of Physical Oceanography*, 30(9):2163–2171.

Hinze, J. O. (1955). Fundamentals of the hydrodynamic mechanism of splitting in dispersion processes. *AIChE Journal*, 1(3):289–295.

Manikantan, H. and Squires, T. M. (2020). Surfactant dynamics: hidden variables controlling fluid flows. *Journal of fluid mechanics*, 892:P1.

Martínez-Bazán, C., Montañés, J. L., and Lasheras, J. C. (1999). On the breakup of an air bubble injected into a fully developed turbulent flow. part 1. breakup frequency. *Journal of Fluid Mechanics*, 401:157–182.

Mazzatenta, M., Erinin, M. A., Néel, B., and Deike, L. (2025). Linking emitted drops to collective bursting bubbles across a wide range of bubble size distributions. *Journal of Fluid Mechanics*, 1015:A8.

Mostert, W., Popinet, S., and Deike, L. (2022). High-resolution direct simulation of deep water breaking waves: transition to turbulence, bubbles and droplets production. *Journal of Fluid Mechanics*, 942.

Ni, R. (2024). Deformation and breakup of bubbles and drops in turbulence. *Annual Review of Fluid Mechanics*, 56(1):319–347.

Pico, P., Kahouadji, L., Shin, S., Chergui, J., Juric, D., and Matar, O. K. (2024). Surfactant-laden bubble bursting: Dynamics of capillary waves and worthington jet at large bond number. *Physical Review Fluids*, 9(8):083606.

Qazi, M. J., Schlegel, S. J., Backus, E. H. G., Bonn, M., Bonn, D., and Shahidzadeh, N. (2020). Dynamic surface tension of surfactants in the presence of high salt concentrations. *Langmuir*, 36(27):7956–7964.

Risso, F. (2018). Agitation, mixing, and transfers induced by bubbles. *Annual Review of Fluid Mechanics*, 50:25–48.

Rivièr, A., Mostert, W., Perrard, S., and Deike, L. (2021). Sub-hinze scale bubble production in turbulent bubble break-up. *Journal of Fluid Mechanics*, 917:A40.

Rivièr, A., Ruth, D. J., Mostert, W., Deike, L., and Perrard, S. (2022). Capillary driven fragmentation of large gas bubbles in turbulence. *Physical Review Fluids*, 7:083602.

Rubio, M. and Montanero, J. M. (2023). Influence of a soluble surfactant on the transition to tip streaming. *Experimental Thermal and Fluid Science*, 141:110776.

Ruth, D. J., Aiyer, A. K., Rivièr, A., Perrard, S., and Deike, L. (2022). Experimental observations and modelling of sub-hinze bubble production by turbulent bubble break-up. *Journal of Fluid Mechanics*, 951:A32.

Sampath, K., Afshar-Mohajer, N., Chandrala, L. D., Heo, W. S., Gilbert, J., Austin, D., Koehler, K., and Katz, J. (2019). Aerosolization of crude oil–dispersant slicks due to bubble bursting. *Journal of Geophysical Research: Atmospheres*, 124(10):5555–5578.

Soligo, G., Roccon, A., and Soldati, A. (2019). Breakage, coalescence and size distribution of surfactant-laden droplets in turbulent flow. *Journal of Fluid Mechanics*, 881:244–282.

Tagawa, Y., Takagi, S., and Matsumoto, Y. (2014). Surfactant effect on path instability of a rising bubble. *Journal of fluid mechanics*, 738:124–142.

- Takemura, F. and Yabe, A. (1999). Rising speed and dissolution rate of a carbon dioxide bubble in slightly contaminated water. *Journal of Fluid Mechanics*, 378:319–334.
- Tasoglu, S., Demirci, U., and Muradoglu, M. (2008). The effect of soluble surfactant on the transient motion of a buoyancy-driven bubble. *Physics of fluids*, 20(4).
- Vejrazka, J., Zedníková, M., and Stanovsky, P. (2018). Experiments on breakup of bubbles in a turbulent flow. *AICHE Journal*, 64(2):740–757.
- Ward, A. F. H. and Tordai, L. (1946). Time-dependence of boundary tensions of solutions i. the role of diffusion in time-effects. *The Journal of Chemical Physics*, 14(7):453–461.
- Yang, Z., Ji, B., Ault, J. T., and Feng, J. (2023). Enhanced singular jet formation in oil-coated bubble bursting. *Nature Physics*, 19:884–890.